THE JOURNAL OF PHYSICAL CHEMISTRY Letters

pubs.acs.org/JPCL Letter

Spectroscopic Study of Sol–Gel Entrapped Triruthenium Dodecacarbonyl Catalyst Reveals Hydride Formation

Joel G. Patrow, Yukun Cheng, Cynthia G. Pyles, Bing Luo, Ian A. Tonks, and Aaron M. Massari*

Cite This: J. Phys. Chem. Lett. 2020, 11, 7394–7399 Read Online

ACCESS | Metrics & More | Article Recommendations | Supporting Information

ABSTRACT: Triruthenium dodecacarbonyl exhibits increased catalytic activity toward hydrogenation reactions when encapsulated in alumina sol–gels. In this study, we demonstrate structural and electronic changes induced by the encapsulation process. Fourier transform infrared (FTIR) spectroscopy reveals that the carbonyl vibrational modes dramatically red shift during aging in the sol–gel glass. These shifts are attributed to the formation of the metal hydride: $[HRu_3(CO)_{11}]^-$. A comparison to the FTIR spectrum of synthesized $[NEt_4][HRu_3(CO)_{11}]$ confirms this assignment. XPS studies show that the Ru $3d_{5/2}$ peak of $[HRu_3(CO)_{11}]^-$ also shifts to lower binding energy, consistent with an increased electron density on the Ru nuclei compared to $Ru_3(CO)_{12}$ and confirmed by density functional calculations. This study should open the door to further investigations into the hydride's role in the previously observed catalytic activity. To the best of our knowledge, this is the first study to identify the presence of $[HRu_3(CO)_{11}]^-$ in the alumina sol–gel.

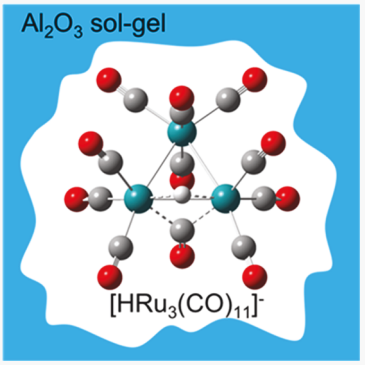

Triruthenium dodecacarbonyl ($Ru_3(CO)_{12}$) has a rich history in chemical catalysis. As a homogeneous catalyst, it has been shown to catalyze the water–gas shift reaction ($CO + H_2O \rightarrow H_2 + CO_2$),[1−3] which plays an important role in the Fischer–Tropsch process.[4] For this reason, $Ru_3(CO)_{12}$ has potential uses in hydrogen based fuel cells in the generation of H_2 and scavenging of CO, which is often found to poison electrode surfaces.[5−7] $Ru_3(CO)_{12}$ is also frequently used as a catalyst in chemical synthesis,[8−12] and it has shown photocatalytic cababilities.[13]

In the realm of heterogeneous catalysis, it is common to find reports of performance enhancement by encapsulating homogeneous catalysts in metal oxide sol–gels.[14] One recent study showed that entrapping $Ru_3(CO)_{12}$ in an alumina sol–gel greatly increased its catalytic activity toward alkene hydrogenation reactions.[15] Curiously, in the same study, it was reported that entrapment of the same catalyst in silica did not affect its catalytic behavior. Increases in catalytic activity upon sol–gel entrapment are common, especially in alumina,[14] but the origins for this effect are not well understood.[16] One possible explanation put forth by the authors of the study is the increased catalytic activity results from the formation of metal hydrides during the sol–gel aging process. Metal hydrides are an important class of catalytic molecules with a plethora of applications in chemical synthesis.[17−19] However, proof of the formation of $[HRu_3(CO)_{11}]^-$ during sol–gel aging was not found. Herein we monitor the FTIR spectra of $Ru_3(CO)_{12}$ during sol–gel formation and report the formation of a new molecular species, $[HRu_3(CO)_{11}]^-$, which likely plays a role in the increased catalytic activity. Our assignment of this species is supported by a separate synthesis of $[NEt_4][HRu_3(CO)_{11}]$ and by density functional theory (DFT) frequency calculations. Complementary X-ray photoelectron spectroscopy (XPS) measurements show that the ruthenium nuclei of $[HRu_3(CO)_{11}]^-$ have increased electron density compared with $Ru_3(CO)_{12}$.

Vibrational Analysis of an Entrapped Hydride. Prior to sol–gel formation, Figure 1a shows that the FTIR spectrum of $Ru_3(CO)_{12}$ in THF exhibits three peaks centered at 2060, 2030, and 2005 cm^{-1}. This spectrum is consistent with previous reports and the features have been assigned to the E′ (axial), A2′ (axial), and E′ (radial) vibrational modes of the carbon monoxide ligands on the complex.[20−22] During the sol–gel synthesis, $Al(O\text{-}i\text{-}Pr)_3$ was hydrolyzed to form a nanoporous alumina (Al_2O_3) network with entrapped $Ru_3(CO)_{12}$. Previous work utilizing N_2–BET analysis reported pore sizes to be on the order of 5 nm.[15] Upon entrapment, the spectral peaks of $Ru_3(CO)_{12}$ decrease while new features that are red-shifted appear. After many hours, the FTIR spectrum in the carbonyl region takes on the appearance shown in Figure 1a (red line). This spectral evolution was monitored as a function of reaction time with spectra obtained every 10 min for 14 h (Figure S2). Comparing the spectra at times $t = 0$ min and $t = 840$ min, an overall red shift of the spectrum by about 43 cm^{-1} is observed with two new peaks present at 1952 and 1733 cm^{-1}. The kinetics of this transformation were quantified

Received: July 28, 2020
Accepted: August 21, 2020
Published: August 21, 2020

https://dx.doi.org/10.1021/acs.jpclett.0c02316
J. Phys. Chem. Lett. 2020, 11, 7394–7399

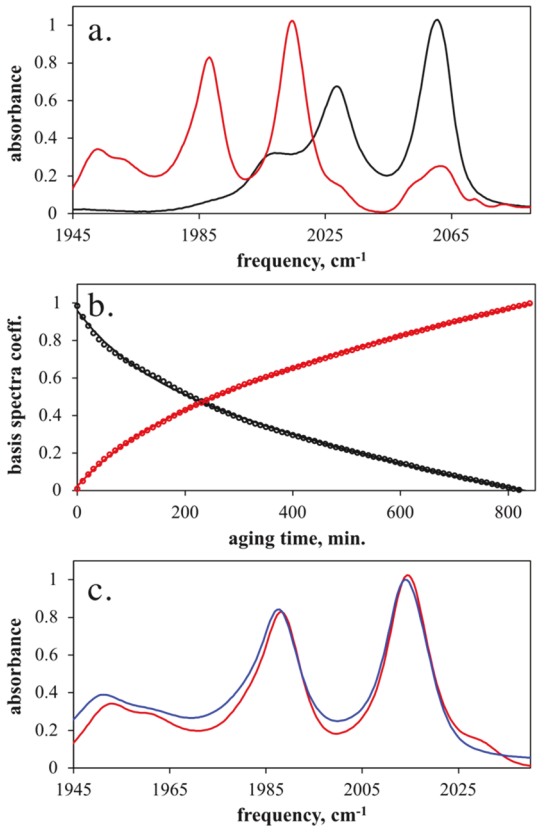

Figure 1. (a) Spectra of $Ru_3(CO)_{12}$ in THF (black) and entrapped in the alumina sol–gel (red). (b) Basis spectra coefficients as a function of sol–gel aging time, as described in the text. Coefficient A (black) is associated with $Ru_3(CO)_{12}$ in THF while coefficient B (red) is associated $Ru_3(CO)_{12}$ in the alumina sol–gel. (c) Spectra of state B (red) and $[NEt_4][HRu_3(CO)_{11}]$ (blue), which confirms state B is $[HRu_3(CO)_{11}]^-$.

with the use of basis spectra defined by fitting the spectral features between 1950 and 2060 cm^{-1} at $t = 0$ min and $t = 840$ min (the first and last spectra obtained) to a sum of eight pseudo-Voigt peak profiles. Each experimental FTIR spectrum in the time lapse data set was then fit to a linear combination of these two basis spectra. The only fit parameters used were the weighting coefficients A (for $Ru_3(CO)_{12}$) and B (for the red-shifted spectrum), whose values were forced to be between 0 and 1 ($0 < A < 1$ and $0 < B < 1$). The time traces of these coefficients along with their global fits are plotted in Figure 1b. The global fit used a biexponential plus a constant offset as its functional form and clearly captures the interconversion dynamics between the two states. The time constants are 100 ± 12 and 1200 ± 200 min. This shows that state A proceeds to state B at two different rates over the course of the sol–gel aging reaction. The source of these two rates is not immediately clear but could be a consequence of environmental effects on the interconversion process. For example, some molecules may find themselves in an environment within the sol–gel matrix where they are more likely to undergo the change from state A to state B compared to others. Such heterogeneous kinetics are complex and warrant further investigation beyond the scope of this work.

Concurrent with the spectral changes in Figure 1, the growth of the peak at 1733 cm^{-1} occurs on a very similar time scale as those observed for the formation of state B (see Figures S2c,d). We conclude that this new peak, which is not observed in the $Ru_3(CO)_{12}$ spectrum, belongs to the same molecular species that produced the spectrum associated with state B.

The spectral changes upon entrapment in the sol–gel are evidence that $Ru_3(CO)_{12}$ molecules undergo a structural change concomitant with the formation of the sol–gel. The 43 cm^{-1} red shift of the carbonyl vibrational peaks is too large to be attributed to a solvatochromic effect.[23−26] Instead, both the red shift and the addition of the two new peaks can be attributed to the formation of $[HRu_3(CO)_{11}]^-$, a metal hydride anion. The increased electron density in the ruthenium d-orbitals from the addition of a hydride ligand could increase π-backbonding with the carbonyl ligands, thereby red-shifting the carbonyl vibrational modes.[25] The fact that $[HRu_3(CO)_{11}]^-$ is a less symmetric molecule than $Ru_3(CO)_{12}$ should increase the number of carbonyl vibrations observable in the IR spectrum. This is consistent with the formation of the two new peaks at 1952 and 1733 cm^{-1}. To confirm that the spectrum of state B belongs to $[HRu_3(CO)_{11}]^-$, we synthesized $[NEt_4][HRu_3(CO)_{11}]$ as a model molecule.[27] Figure 1c shows that the vibrational spectrum of state B and $[NEt_4][HRu_3(CO)_{11}]$ are identical, confirming the assignment of state B to $[HRu_3(CO)_{11}]^-$. For completeness, vibrational frequency computations of $Ru_3(CO)_{12}$ and $[HRu_3(CO)_{11}]^-$ were also performed. These results are consistent with experiment and can be found in the Supporting Information.

The structure of the ruthenium hydride, as determined previously by X-ray crystallography[27] is similar to that of $Ru_3(CO)_{12}$.[28] The DFT-optimized structures of both molecules are displayed in Figure 2. The structural changes most

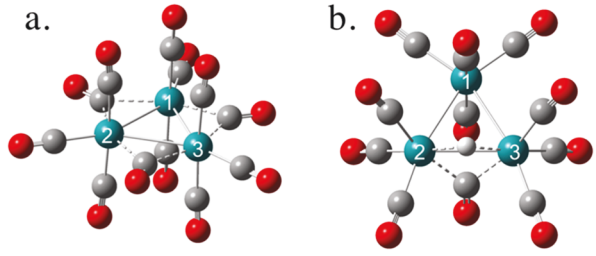

Figure 2. Optimized structures of (a) $Ru_3(CO)_{12}$ and (b) $[HRu_3(CO)_{11}]^-$.

relevant to this work are the presence of the bridging carbonyl and bridging hydride between ruthenium nuclei 2 and 3 (Ru-2 and Ru-3) in $[HRu_3(CO)_{11}]^-$. As previously shown, the bridging carbonyl in $[HRu_3(CO)_{11}]^-$ is red-shifted from the other carbonyl modes to around 1700 cm^{-1}.[27] This is also consistent with our frequency calculations that predict the bridging carbonyl mode to be red-shifted from the other carbonyl modes (see Supporting Information). On the basis of these findings, the peak at 1733 cm^{-1} is likely the bridging carbonyl. We further support this claim by ruling out the possibility it could be the Ru–H–Ru stretch mode. We performed sol–gel entrapment using D_2O and synthesized $[NEt_4][DRu_3(CO)_{11}]$. Spectra of both samples contain the peak at 1733 cm^{-1} (Figure S4). Therefore, we assign this peak to the bridging carbonyl. For completeness, we have included the spectrum of $[NEt_4][DRu_3(CO)_{11}]$, which is identical to the spectrum for $[NEt_4][HRu_3(CO)_{11}]$ in the region from 1600 to 2060 cm^{-1} (Figure S5).

Population analyses of $Ru_3(CO)_{12}$ and $[HRu_3(CO)_{11}]^-$ were performed on the DFT optimized structures. The results are displayed in Table 1. The net Mulliken charge on the

https://dx.doi.org/10.1021/acs.jpclett.0c02316
J. Phys. Chem. Lett. 2020, 11, 7394−7399

Table 1. Net Mulliken and APT Charges on the Nuclei and Ligands in $Ru_3(CO)_{12}$ and $[HRu_3(CO)_{11}]^-$

	$Ru_3(CO)_{12}$		$[HRu_3(CO)_{11}]^-$	
	Mulliken	APT	Mulliken	APT
Ru-1	−0.22	−1.59	−0.15	−1.90
Ru-2	−0.22	−1.59	−0.25	−1.63
Ru-3	−0.22	−1.59	−0.25	−1.63
CO[a]	0.67	4.76	−0.61	4.04
H			0.15	0.12

[a]For the CO ligands, instead of listing out the Mulliken charges for every carbon and oxygen nuclei, we list the summed net charge on all of the carbon and oxygen nuclei combined.

carbonyl ligands changes by −1.28 while the atomic polar tensor (APT) changes by −0.72; the electron density on the carbonyl ligands increases upon transformation from $Ru_3(CO)_{12}$ to $[HRu_3(CO)_{11}]^-$. When π-backbonding occurs, electron density from the metal is donated to the π^* antibonding orbital of the CO ligand, which weakens the CO bonds and causes the carbonyl vibrational modes to red shift. The increased electron density exemplified by the Mulliken and APT charge analysis confirm π-backbonding is the source of the red shift of the carbonyl modes.

This work provides the first conclusive experimental evidence that $Ru_3(CO)_{12}$ is spontaneously converted to $[HRu_3(CO)_{11}]^-$ in an alumina sol−gel. Although this finding is remarkable, it is not necessarily surprising. Ruthenium metal hydrides have also been suggested to form when $Ru_3(CO)_{12}$ is adsorbed onto the surface of alumina supports.[29,30] In these cases, the formation of the hydride was correlated with whether or not the alumina surfaces had been dehydroxylated. Formation of the ruthenium hydride was hypothesized to occur when alumina surfaces retained their hydroxyl groups. Therefore, it is possible in this case that the formation of OH groups on the sol−gel surface during the sol−gel process are responsible for the formation of $[HRu_3(CO)_{11}]^-$.

The formation of a ruthenium hydride undoubtedly has consequences regarding the increased catalytic activity of the sol-entrapped ruthenium molecule. In homogeneous catalysis, ruthenium hydrides play an important role in hydrogenation reactions.[31,32] It is possible that the ruthenium hydride here is the catalytically active species responsible for the previously observed increased catalytic activity in the entrapped ruthenium molecule. At the very least, the fact that it is observed to form during the sol−gel aging process places it as an important precursor in the catalytic reaction. If it is, indeed, the catalytically active species, it is worth noting this could lead to faster reaction kinetics compared to processes requiring catalyst activation as a necessary step in the chemical reaction.

Electronic Redistribution Inside the Sol−Gel Matrix. To better understand how the electronic distribution changes upon formation of $[HRu_3(CO)_{11}]^-$, XPS spectra of $Ru_3(CO)_{12}$ and $[HRu_3(CO)_{11}]^-$ entrapped in the alumina sol−gel were collected (Figure 3). Because Ru 3d peaks overlap with C 1s peaks, the conventional method using adventitious carbon as the energy reference was not applicable. We chose to add a small amount of CaF_2 in the samples and used the Ca $2p_{3/2}$ at 349.0 eV[33] as the reference. The high-resolution spectra of CaF_2 in all samples exhibited well-defined doublets for Ca 2p and singlets for F 1s and nearly identical peak locations, indicating there was no measurable interaction between CaF_2 and the samples and that this referencing method was valid.

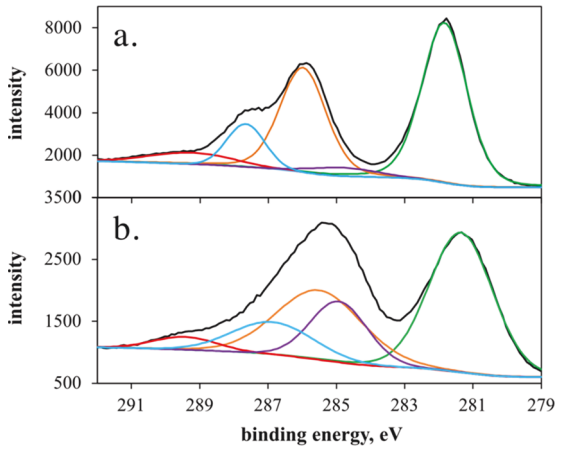

Figure 3. XPS spectra of Ru 3d and C 1s orbitals for (a) crystalline $Ru_3(CO)_{12}$ and (b) $[HRu_3(CO)_{11}]^-$. In both spectra, the green peaks are the Ru $3d_{5/2}$ and the yellow peaks are the Ru $3d_{3/2}$; the purple peaks are adventitious carbon, and the light blue peaks are the C 1s peaks associated with the CO ligands.

XPS data on ruthenium-containing molecules is not extensive;[34] there are no previously reported spectra of $[HRu_3(CO)_{11}]^-$. The ruthenium $3d_{5/2}$, $3d_{3/2}$ and carbonyl C 1s peaks are observed at binding energies of 281.8 and 281.3 eV, 286.0 and 285.5, and 287.8 and 287.0 eV for $Ru_3(CO)_{12}$ and $[HRu_3(CO)_{11}]^-$, respectively (for a complete list of peak positions see the Supporting Information). This red shift in binding energy between $Ru_3(CO)_{12}$ and $[HRu_3(CO)_{11}]^-$ is consistent with the idea that the hydride increases the electron density on the ruthenium atoms and carbonyl ligands. More electron density on a nucleus decreases the binding energy of the electrons because of an increase in the repulsion among the electrons on the nuclei. Interestingly, the population analyses (Table 1) show that the charge is unevenly distributed among the Ru nuclei with Ru-1 (not associated with the bridging hydride in Figure 2) being different from Ru-2 and Ru-3. For $[HRu_3(CO)_{11}]^-$ the Mulliken charges on the two equivalent Ru-2 and Ru-3 nuclei decrease (slightly) compared to $Ru_3(CO)_{12}$; however, the Mulliken charge on Ru-1 increases, indicating less electron density on that atom. This would necessitate a second Ru $3d_{5/2}$ peak in the $[HRu_3(CO)_{11}]^-$ XPS spectrum that is blue-shifted from the Ru $3d_{5/2}$ peak observed in the $Ru_3(CO)_{12}$ spectrum. This is not observed experimentally. In contrast to the Mulliken charge analysis, the APT charges on the Ru nuclei all decrease compared to $Ru_3(CO)_{12}$, indicating an increase in electron density. This electronic change is confirmed by the experimental XPS results. Comparing the APT charges on the Ru nuclei to the net charge density on the CO ligands, it is striking that more electron density from the hydride is donated to the CO ligands than ends up on the Ru nuclei. Concomitant with an increase in catalytic activity upon sol−gel entrapment, we conclude that there is a disproportionate distribution of excess charge onto the peripheral ligands rather than the ruthenium atoms.

We also note that the Ru 3d and carbonyl C 1s peaks associated with $[HRu_3(CO)_{11}]^-$ in the sol−gel are broader than for $Ru_3(CO)_{12}$. This is certainly a consequence of the fact that the atoms are electronically more heterogeneous in the hydride structure but may also be influenced by an increase in heterogeneity of solvation environments within the sol−gel. We hypothesize that this is related to the multiexponential

https://dx.doi.org/10.1021/acs.jpclett.0c02316
J. Phys. Chem. Lett. 2020, 11, 7394−7399

kinetics observed in the FTIR evolution described above. We will address this solvation heterogeneity as it pertains the IR spectrum of the carbonyl ligands in a forthcoming publication.

In closing, we find here that entrapment of $Ru_3(CO)_{12}$ in an alumina sol−gel causes distinct spectral shifts of the carbonyl modes and the addition of two new peaks that are assigned to the formation of $[HRu_3(CO)_{11}]^-$. To the best of our knowledge, this is the first direct evidence of ruthenium hydride formation in a sol−gel film. The kinetics of the sol−gel aging process were followed via FTIR and show that there are two distinct pathways to formation of the entrapped $[HRu_3(CO)_{11}]^-$. This is likely a manifestation of heterogeneous environments in the sol−gel that affect the rate of conversion from $Ru_3(CO)_{12}$ to $[HRu_3(CO)_{11}]^-$. Future work should identify whether $[HRu_3(CO)_{11}]^-$ is the catalytic species responsible for the observed increase in hydrogenation activity. In addition to the FTIR analysis, XPS spectra of $Ru_3(CO)_{12}$ and $[HRu_3(CO)_{11}]^-$ entrapped in the alumina sol−gel were obtained for the first time. Paired with computational results, we show that the increased electron density from the hydride is distributed unevenly onto the carbonyl ligands and ruthenium nuclei. This is fully consistent with the red-shifted spectral features of the FTIR and XPS data. This work provides conclusive identification of reactive intermediates that form in the interior of alumina sol−gel pores and is an important step toward understanding enhanced activity of catalysts entrapped in sol−gel materials.

EXPERIMENTAL METHODS

Materials. $Ru_3(CO)_{12}$, aluminum isopropoxide ($Al(O\text{-}i\text{-}Pr)_3$), and tetrahydrofuran (THF) used for alumina sol−gel studies were purchased from Millipore-Sigma and used as received. $Ru_3(CO)_{12}$, sodium borohydride ($NaBH_4$), and sodium borodeuteride ($NaBD_4$) used in the air and moisture sensitive synthesis of $[NEt_4][HRu_3(CO)_{11}]$ and $[NEt_4][DRu_3(CO)_{11}]$ were purchased from Millipore-Sigma and dried in vacuo prior to use. The solvents used in the synthesis of $[NEt_4][HRu_3(CO)_{11}]$ (THF, pentane, dichloromethane, and Et_2O) were dried through activated alumina on a Pure Process Technology solvent purification system.

Sol−Gel Formation. $Ru_3(CO)_{12}$ alumina sol−gels were prepared according to a previous procedure.[15] Approximately 0.02 mmol of $Ru_3(CO)_{12}$ was dissolved in 1 mL of THF and stirred. Separately, approximately 6 mmol of $Al(O\text{-}i\text{-}Pr)_3$ was dissolved in 4 mL of THF, which was then decanted into the stirring $Ru_3(CO)_{12}$ solution. The mixture was then stirred for 20 min. For the FTIR kinetic study, approximately 1 mL of deionized water was added to the stirring $Ru_3(CO)_{12}$/$Al(O\text{-}i\text{-}Pr)_3$ mixture. Upon addition of the water, the mixture went from a transparent yellow to an opaque yellow. Immediately after adding water, a small aliquot of the mixture was transferred to a sample cell composed of two CaF_2 windows separated by a 50 μm Teflon spacer. The assembly was then sealed together with epoxy resin along its edges. The epoxy was allowed to dry for 20 min before any measurements were performed.

Synthesis of $[NEt_4][HRu_3(CO)_{11}]$. $[NEt_4][HRu_3(CO)_{11}]$ and $[NEt_4][DRu_3(CO)_{11}]$ were synthesized via a modified literature procedure.[27] In a glovebox, $Ru_3(CO)_{12}$ (106 mg, 0.166 mmol), $NaBH_4$ (33 mg, 0.87 mmol), and 17 mL of THF were added to a 20 mL scintillation vial along with a small stir bar. The reaction was then sealed with a Teflon screw cap and stirred for 40 min at room temperature. $[Et_4N]Br$ (42 mg, 0.20 mmol) was then added to the solution, and the reaction was stirred for another 1 h. The solution was filtered through a pipet plug and concentrated to 2 mL by vacuum. Fifteen milliliters pentane was added to the solution, forming a precipitate. The resulting suspension was filtered, and the precipitate was washed with 2 mL of pentane. The precipitate was then dissolved in CH_2Cl_2, and crystallization of $[NEt_4][HRu_3(CO)_{11}]$ was achieved by vapor diffusion of Et_2O into CH_2Cl_2, yielding $[NEt_4][HRu_3(CO)_{11}]$ as reddish-brown crystals. Yield: 95 mg (0.13 mmol, 77%). A similar procedure using $NaBD_4$ (stirred for 2 h instead of 40 min) yielded $[NEt_4][DRu_3(CO)_{11}]$ (65 mg, 0.087 mmol, 53%). See the Supporting Information for the ^1H NMR spectrum.

FTIR Measurements. FTIR spectra were collected using a Nicolet 6700 FTIR spectrometer (Thermo Scientific). The resolution was 1 cm^{-1} with an average of 16 scans. The spectrum of $Ru_3(CO)_{12}$ in THF was collected with THF as the background. The spectra of $Ru_3(CO)_{12}$ entrapped in the alumina sol−gel as well as $[NEt_4][HRu_3(CO)_{12}]$ were collected with a background of air. For $[NEt_4][HRu_3(CO)_{11}]$, because the synthesis is air sensitive, the FTIR sample was prepared in a glovebox and then brought quickly to the FTIR spectrometer to avoid degradation.

XPS Measurements. XPS measurements were performed on a PHI Versa Probe III XPS system (ULVAC-PHI) using a monochromated Al Kα X-ray source (1486.6 eV). The base pressure was 4.0×10^{-8} Pa. During data collection, the pressure was ca. 2.0×10^{-6} Pa. The crystalline and sol−gel samples included a small amount of CaF_2 powder to serve as an internal reference. All samples were mounted on the holder using a piece of sticking tape. The measurements were conducted using an X-ray spot size of 0.1×0.1 mm^2 with a power of 25 W under 15 kV. Charge neutralization was used. The survey spectra were measured using 280 eV pass energy and 1.0 eV/step. The high resolution spectra were collected using 55 eV pass energy and 0.1 eV/step. The data processing used the Multipak software. Energies were referenced to the Ca $2p_{3/2}$ peak at 349.0 eV.[33]

Computations. DFT geometry optimizations, frequency computations, and population analyses were performed using B3LYP as the functional. The LanL2DZ pseudopotential basis set was used for the Ru atoms while the 6-31G(d) was used for C, O, and H atoms. The frequencies were multiplied by a DFT scaling factor (0.960).[35,36] All computations were performed with Gaussian.[37]

ASSOCIATED CONTENT

Supporting Information

The Supporting Information is available free of charge at https://pubs.acs.org/doi/10.1021/acs.jpclett.0c02316.

^1H NMR spectrum of $[NEt_4][HRu_3(CO)_{11}]$; detailed FTIR spectra during sol−gel aging; DFT computed vibrational analysis; complete list of XPS binding energies (PDF)

AUTHOR INFORMATION

Corresponding Author

Aaron M. Massari − *University of Minnesota—Twin Cities, Minneapolis, Minnesota 55454, United States;* orcid.org/0000-0003-2089-9933; Email: massari@umn.edu

https://dx.doi.org/10.1021/acs.jpclett.0c02316
J. Phys. Chem. Lett. 2020, 11, 7394−7399

Authors

Joel G. Patrow − *University of Minnesota—Twin Cities, Minneapolis, Minnesota 55454, United States*

Yukun Cheng − *University of Minnesota—Twin Cities, Minneapolis, Minnesota 55454, United States;* orcid.org/0000-0002-2379-9404

Cynthia G. Pyles − *University of Minnesota—Twin Cities, Minneapolis, Minnesota 55454, United States*

Bing Luo − *University of Minnesota—Twin Cities, Minneapolis, Minnesota 55454, United States*

Ian A. Tonks − *University of Minnesota—Twin Cities, Minneapolis, Minnesota 55454, United States;* orcid.org/0000-0001-8451-8875

Complete contact information is available at: https://pubs.acs.org/10.1021/acs.jpclett.0c02316

Notes

The authors declare no competing financial interest.

■ ACKNOWLEDGMENTS

The authors gratefully acknowledge partial support from the National Science Foundation under CHE-1464416 and CHE-1611047. J.G.P. was supported in part by a Mistletoe Research Fellowship. C.G.P. was supported in part by a Newman and Lillian Bortnick Fellowship. Parts of this work were carried out in the Characterization Facility, University of Minnesota, which receives partial support from NSF through the MRSEC program.

■ REFERENCES

(1) Ford, P. C. The Water Gas Shift Reaction: Homogeneous Catalysis by Ruthenium and Other Metal Carbonyls. *Acc. Chem. Res.* **1981**, *14*, 31−37.

(2) Laine, R. M.; Rinker, R. G.; Ford, P. C. Homogeneous Catalysis by Ruthenium Carbonyl in Alkaline Solution: The Water Gas Shift Reaction. *J. Am. Chem. Soc.* **1977**, *99*, 252−253.

(3) Liu, N.; Guo, L.; Cao, Z.; Li, W.; Zheng, X.; Shi, Y.; Guo, J.; Xi, Y. Mechanisms of the Water-Gas Shift Reaction Catalyzed by Ruthenium Carbonyl Complexes. *J. Phys. Chem. A* **2016**, *120*, 2408−2419.

(4) Owen, J. Coal Liquefaction. *Appl. Sci. Res.* **1979**, 53−65.

(5) Choi, Y.; Stenger, H. G. Water Gas Shift Reaction Kinetics and Reactor Modeling for Fuel Cell Grade Hydrogen. *J. Power Sources* **2003**, *124*, 432−439.

(6) Smith R J, B.; Loganathan, M.; Shantha, M. S. A Review of the Water Gas Shift Reaction Kinetics. *Int. J. Chem. React. Eng.* **2010**, *8*. DOI: 10.2202/1542-6580.2238

(7) Tanaka, Y.; Utaka, T.; Kikuchi, R.; Takeguchi, T.; Sasaki, K.; Eguchi, K. Water Gas Shift Reaction for the Reformed Fuels over Cu/Mno Catalysts Prepared Via Spinel-Type Oxide. *J. Catal.* **2003**, *215*, 271−278.

(8) Chatani, N.; Fukuyama, T.; Kakiuchi, F.; Murai, S. Ru3(Co)12-Catalyzed Coupling of Heteroaromatic C-H/Co/Olefins. Regioselective Acylation of the Imidazole Ring. *J. Am. Chem. Soc.* **1996**, *118*, 493−494.

(9) Fleischer, I.; Wu, L.; Profir, I.; Jackstell, R.; Franke, R.; Beller, M. Towards the Development of a Selective Ruthenium-Catalyzed Hydroformylation of Olefins. *Chem. - Eur. J.* **2013**, *19*, 10589−10594.

(10) Ie, Y.; Chatani, N.; Ogo, T.; Marshall, D. R.; Fukuyama, T.; Kakiuchi, F.; Murai, S. Direct Carbonylation at a C-H Bond in the Benzene Ring of 2- Phenyloxazolines Catalyzed by Ru3(Co)12. Scope, Limitations, and Mechanistic Aspects. *J. Org. Chem.* **2000**, *65*, 1475−1488.

(11) Kim, D. S.; Park, W. J.; Lee, C. H.; Jun, C. H. Hydroesterification of Alkenes with Sodium Formate and Alcohols Promoted by Cooperative Catalysis of Ru3(Co)12 and 2-Pyridinemethanol. *J. Org. Chem.* **2014**, *79*, 12191−12196.

(12) Kang, S. K.; Kim, K. J.; Hong, Y. T. Synthesis of Alpha-Methylene-Gamma-Butyrolactones: Ru-Catalyzed Cyclocarbonylation of Allenyl Aldehydes and Allenyl Ketones. *Angew. Chem., Int. Ed.* **2002**, *41*, 1584−1586.

(13) Gafney, H. D.; Xu, S. P. Photocatalyzed Isomerization of 1-Pentene by Ru3(Co)12 Adsorbed onto Porous Vycor Glass. *Inorg. Chim. Acta* **1995**, *240*, 645−651.

(14) Blum, J.; Avnir, D. *Handbook of Sol-Gel Science and Technology. Processing Characterization and Application. Vol. Iii: Applications of Sol-Gel Technology.*; Kluwer Academic Publishers: Norwell, 2005; pp 507−550.

(15) Eliau, N.; Avnir, D.; Eisen, M. S.; Blum, J. Activation of Metal-Carbonyl Clusters by Their Encapsulation within Alumina Sol-Gel Matrices. *J. Sol-Gel Sci. Technol.* **2005**, *35*, 159−167.

(16) Marr, A. C.; Marr, P. C. Entrapping Homogeneous Catalysts by Sol-Gel Methods: The Bottom-up Synthesis of Catalysts That Recycle and Cascade. *Dalton Trans* **2011**, *40*, 20−26.

(17) Crabtree, R. H. *The Organometallic Chemistry of the Transition Metals*, 5th ed.; John Wiley & Sons, 2009.

(18) Lau, C. P.; Ng, S. M.; Jia, G.; Lin, Z. Some Ruthenium Hydride, Dihydrogen, and Dihydrogen-Bonded Complexes in Catalytic Reactions. *Coord. Chem. Rev.* **2007**, *251*, 2223−2237.

(19) Nagashima, H. Facile Hydrogenation of Acenapthylenes and Azulenes on the Face of a Triruthenium Carbonyl Moiety: Discovery of Specific Reactions on the Cluster Framework Providing Unique Insight for Cluster Catalysis. *Monatsh. Chem.* **2000**, *131*, 1225−1239.

(20) Battiston, G. A.; Sbrignadello, G.; Bor, G.; Dietler, U. K.; Kettle, S. F. A.; Rossetti, R.; Luigi, P. S. Comparative Infrared and Raman Spectroscopic P(Co) Study of Ru3(Co)12, Os3(Co)12, Their Mixed Crystals, and the Mixed Triangulo Cluster Carbonyls Ru2os(Co)I2 and Ruos2(Co)J2la. *Inorg. Chem.* **1980**, *19*, 1961−1973.

(21) Battiston, G. A.; Sbrignadello, G.; Bork, G. Infrared Spectroscopic Studies on Metal Carbonyl Compounds. 23.La a Simple Quantitative Treatment of the Infrared Band Intensity and the Induced Metal-Metal Dipole Contribution to It in Polynuclear Metal Carbonyls. An Application to the Spectrum of Ru3(Co)12. *Inorg. Chem.* **1980**, *19*, 1973−1977.

(22) Dong, X.; Yang, F.; Zhao, J.; Wang, J. Efficient Intramolecular Vibrational Excitonic Energy Transfer in Ru3(Co)12 Cluster Revealed by Two-Dimensional Infrared Spectroscopy. *J. Phys. Chem. B* **2018**, *122*, 1296−1305.

(23) Choi, J. H.; Cho, M. Vibrational Solvatochromism and Electrochromism of Infrared Probe Molecules Containing C≡O, C≡N, C = O, or C-F Vibrational Chromophore. *J. Chem. Phys.* **2011**, *134*, 154513.

(24) Fried, S. D.; Boxer, S. G. Measuring Electric Fields and Noncovalent Interactions Using the Vibrational Stark Effect. *Acc. Chem. Res.* **2015**, *48*, 998−1006.

(25) Huber, C. J.; Anglin, T. C.; Jones, B. H.; Muthu, N.; Cramer, C. J.; Massari, A. M. Vibrational Solvatochromism in Vaska's Complex Adducts. *J. Phys. Chem. A* **2012**, *116*, 9279−9286.

(26) Levinson, N. M.; Fried, S. D.; Boxer, S. G. Solvent-Induced Infrared Frequency Shifts in Aromatic Nitriles Are Quantitatively Described by the Vibrational Stark Effect. *J. Phys. Chem. B* **2012**, *116*, 10470−10476.

(27) Johnson, B. F. G.; Lewis, J.; Raithby, P. R.; Süss, G. The Triruthenium Cluster Anion [Ru3h(Co)11]-: Preparation, Structure and Fluxionlity. *J. Chem. Soc., Dalton Trans.* **1979**, 1356−1361.

(28) Churchill, M. R.; Hollander, F. J.; Hutchinson, J. P. An Accurate Redetermination of the Structure of Triruthenium Dodecacarbonyl, Ru3(Co)12. *Inorg. Chem.* **1977**, *16*, 2655−2659.

(29) Asakura, K.; Bando, K. K.; Iwasawa, Y. Structure and Behaviour of Ru3(Co)12 Supported on Inorganic Oxide Surfaces, Studied by Exafs, Infrared Spectroscopy and Temperature-Programmed Decomposition. *J. Chem. Soc., Faraday Trans.* **1990**, *86*, 2645−2655.

(30) Kuznetsov, V. L.; Bell, A. T.; Yermakov, Y. I. An Infrared Study of Alumina- and Silica-Supported Ruthenium Cluster Carbonyls. *J. Catal.* **1980**, *65*, 374−389.
(31) Clapham, S. E.; Hadzovic, A.; Morris, R. H. Mechanisms of the H2-Hydrogenation and Transfer Hydrogenation of Polar Bonds Catalyzed by Ruthenium Hydride Complexes. *Coord. Chem. Rev.* **2004**, *248*, 2201−2237.
(32) Conley, B. L.; Pennington-Boggio, M. K.; Boz, E.; Williams, T. J. Discovery, Applications, and Catalytic Mechanisms of Shvos Catalyst. *Chem. Rev.* **2010**, *110*, 2294−2312.
(33) Seyama, H.; Soma, M. X-Ray Photoelectron Spectroscopic Study of Montmorillonite Containing Exchangeable Divalent Cations. *J. Chem. Soc., Faraday Trans. 1* **1984**, *80*, 237−248.
(34) Nist X-Ray Photoelectron Spectroscopy Database. In *NIST Standard Reference Database Number 20*; National Institute of Standards and Technology: Gaithersburg, MD, 2000; Vol. *20899*.
(35) Johnson, R. D., III. NIST Computational Chemistry Comparison and Benchmark Database. In *NIST Standard Reference Database Number 101*; National Institute of Standards and Technology: Gaithersburg, MD, 2019; Vol. *20*.
(36) Scott, A. P.; Radom, L. Harmonic Vibrational Frequencies: An Evaluation of Hartree-Fock, Møller-Plesset, Quadratic Configuration Interaction, Density Functional Theory, and Semiempirical Scale Factors. *J. Phys. Chem.* **1996**, *100*, 16502−16513.
(37) Frisch, M. J.; Trucks, G. W.; Schlegel, H. B.; Scuseria, G. E.; Robb, M. A.; Cheeseman, J. R.; Scalmani, G.; Barone, V.; Petersson, G. A.; Nakatsuji, H.; et al. *Gaussian 16*; Gaussian, Inc.: Wallingford, CT, 2016.

https://dx.doi.org/10.1021/acs.jpclett.0c02316
J. Phys. Chem. Lett. 2020, 11, 7394−7399